PERGAMON

Pattern Recognition 32 (1999) 1351–1368

PATTERN RECOGNITION
THE JOURNAL OF THE PATTERN RECOGNITION SOCIETY

# Robust voxel similarity metrics for the registration of dissimilar single and multimodal images

Christophoros Nikou[a,b,*], Fabrice Heitz[a], Jean-Paul Armspach[b]

[a] *Université Louis Pasteur (Strasbourg I), Laboratoire des Sciences de l'Image, de l'Informatique et de la Télédétection UPRES-A CNRS 7005, 4, Bd. Sébastien Brant, 67400 Illkirch, France*

[b] *Université Louis Pasteur (Strasbourg I), Institut de Physique Biologique, Faculté de Médecine, CNRS-UPRES-A 7004, 4 rue Kirschleger, 67085 Strasbourg France*

Received 13 April 1998; received in revised form 9 November 1998, accepted 9 November 1998

**Abstract**

In this paper, we develop data driven registration algorithms, relying on pixel similarity metrics, that enable an accurate (subpixel) rigid registration of dissimilar single or multimodal 2D/3D images. Gross dissimilarities are handled by considering similarity measures related to robust M-estimators. In particular, a novel (robust) similarity metric is proposed for comparing multimodal images. The proposed robust similarity metrics are compared to the most popular standard similarity metrics, on synthetic as well as on real-world image pairs showing gross dissimilarities. Three case studies are considered: the registration of single modal and multimodal 3D medical images, the matching of multispectral remotely sensed images, and the registration of intensity and range images. The proposed robust similarity measures compare favourably with the standard (non-robust) techniques. © 1999 Pattern Recognition Society. Published by Elsevier Science Ltd. All rights reserved.

*Keywords*: Single and multimodal image registration; Dissimilar image registration; Similarity metrics; Robust estimation

## 1. Introduction

The goal of image registration is to geometrically align two or more images so that pixels (or voxels) representing the same underlying structure may be superimposed. Image registration is an important preliminary step in many application fields involving, for instance, the detection of changes in temporal image sequences or the fusion of multimodal images [1]. Medical imaging, with its wide variety of sensors (thermal, ultrasonic, X-ray, MRI and nuclear) is probably one of the first application field, as are remote sensing, military imaging (visible, IR or radar), multisensor robot vision and multisource imaging used in the preservation of artistic patrimony. Applications include the following of the evolution of lesions in medical image sequences [2], the detection of changes in urban development from aerial photographs [3] and the recovery of underpaintings from visible/X-ray pairs of images in fine arts painting analysis [4].

Most change detection or data fusion algorithms assume that the images to be compared are perfectly registered. Even slight misregistrations may become an important source of interpretation errors when

*Corresponding author. Tel.: +33 3 88 65 50 51; Fax: +33 3 88 65 52 49; E-mail: nikou@mondrian.u-strasbg.fr


PII: S0031-3203(98)00167-8

interimage changes have to be detected. Accurate (i.e. subpixel or subvoxel) registration of single-modal images remains an intricate problem when gross dissimilarities are observed.

Gross dissimilarities may be large lesion evolution for multiple sclerosis patients (Fig. 7), functional information in SPECT images not presented in MRI for patients with partial epilepsy (Fig. 9), large areas covered with clouds in remotely sensed images (Fig. 11), images that do not completely overlap (pre- post-operative brain images, skull and scalp structures in MRI not present in functional imaging (Fig. 10). The problem is even more difficult for multimodal images, showing both localized changes that have to be detected [4] and an "overall" difference (due to differences in the characteristics of the scene observed by multiple sensors).

Although a large variety of image registration methods have been proposed in the literature, only a few techniques have attempted to address the registration of images showing gross dissimilarities. If the case of single-modal dissimilar images has been considered [2], to our knowledge, no specific model has been proposed to handle *multimodal images* exhibiting large dissimilarities.

In the present paper, we develop several data driven registration methods, relying on pixel (or voxel) similarity metrics, that enable an accurate (subpixel) rigid registration of dissimilar single or multimodal 2D/3D images. Gross dissimilarities are handled by considering similarity measures related to robust M-estimators. In particular, a novel pixel similarity metric is proposed for the multimodal case. This metric has shown very efficient for the registration of highly dissimilar images, on which conventional techniques fail. An example of such a multimodal image pair is given in Fig. 11, showing two satellite images of France, taken at different optical wavelengths and at different dates. Gross dissimilarities, due to the presence of large overcast areas may be observed. Subpixel registrations have been obtained in this case (see Section 4).

The remainder of this paper is organized as following. Background and related approaches are presented in Section 2. In Section 3, we introduce two robust similarity metrics for the registration of single and multimodal images. The data-driven registration algorithm, based on these robust similarity measures, is described in the same section. In Section 4, the robust similarity metrics are compared to the most popular standard similarity metrics, on synthetic as well as on real-world image pairs showing gross dissimilarities. The registration accuracy is evaluated for three case studies: the registration of single modal (MRI/MRI) and multimodal (MRI/SPECT) 3D medical images, the matching of multispectral (visible/IR) satellite images showing large overcast areas and the registration of intensity and range stereo images. The proposed robust similarity measures compare favourably with all standard (non-robust) techniques (including the quadratic similarity measure and the multimodality registration criterion devised by Woods et al. [5]. The multimodal robust similarity metrics shows also (excepted for one particular case) better performances than the recently proposed mutual information criterion [6,7], that has been recognized as the most efficient method in several recent studies [8].

## 2. Background and standard similarity measures

### 2.1. Related work

A complete review of standard registration techniques has been made by Brown [1]. Similarity measure-based approaches rely on the minimization of cost functions that express the pixel or voxel similarity of the images to be aligned. They have been proposed for both single and multimodal image registration. Standard similarity metrics are related to least-squares estimation [9–11] or to the maximization of the correlation function [12]. Other similarity measures, based on first- or second-order image statistics such as mean, variance [13,5], entropy measures [6,7], or texture moments [14] have also been devised.

Similarity metrics for the registration of 2D single-modal images, that are to a certain extent robust to image changes have been described by Herbin et al. [2]. Herbin et al. make use of deterministic and stochastic sign change criteria to obtain robust registrations of medical image sequences in critical situations corresponding, for instance, to lesion evolutions [2]. A robust statistics-based approach, has been proposed recently and independently [15] for the registration of 2D single-modal images. The approach of Alexander et al. [15] uses sparse features (edges) extracted from the image pair and relies on a least median of squares robust estimator [16]. Contrary to the metrics described below, these methods do not handle the case of multimodal images.

### 2.2. Standard similarity metrics

In this section we briefly present a selection of the most popular similarity metrics and describe their limitations. These similarity metrics will be compared, in Section 4, to the robust metrics we propose.

Pixel (or voxel) similarity metric-based registration consists in estimating the parameters $\Theta$ of the rigid transformation $T_\Theta$ minimizing a cost function $E(I_{\text{ref}}(\cdot), I_{\text{reg}}(T_\Theta(\cdot)))$, that expresses the similarity between the single or multimodal image pair

$$\Theta^* = \arg\min_{\Theta} [E(I_{\text{ref}}(\cdot), I_{\text{reg}}(T_\Theta(\cdot)))], \tag{1}$$

where (for 3D images)

$$\Theta = (t_x, t_y, t_z, \hat{\theta}_x, \hat{\theta}_y, \hat{\theta}_z)^{\mathrm{T}} \tag{2}$$

is a vector containing the 3D translation parameters $(t_x, t_y, t_z)$ with respect to the $X,Y$ and $Z$ axis and the Euler rotation angles $(\hat{\theta}_x, \hat{\theta}_y, \hat{\theta}_z)$. $I_{\text{ref}}(\cdot)$ represents the reference image and $I_{\text{reg}}(\cdot)$ the image to be registered.

A classical similarity measure, widely used for the registration of single-modal images is the quadratic similarity measure [9,11]. This similarity metric assumes that the two registered images differ only by an additive Gaussian noise [10], leading to the following *least-squares cost function*:

$$E(I_{\text{ref}}(\cdot), I_{\text{reg}}(T_\Theta(\cdot))) = \sum_x [I_{\text{ref}}(x) - I_{\text{reg}}(T_\Theta(x))]^2, \tag{3}$$

where $x$ designates the pixel (or voxel) coordinates. Quadratic similarity metrics are related to Gaussian sensor models [10], which do not take into account the interimage dissimilarities that may occur in real-world applications.

A popular similarity measure for the registration of multimodal image pairs (widely used in medical imaging) is the multimodality similarity metric devised by Woods et al. [5]. The fundamental assumption related to Woods criterion is that a uniform region in the reference image corresponds, after registration, to a region that is also uniform in the second image (inter-image uniformity hypothesis).

The reference image is thus first partitioned into $G$ grey-level classes, where $G$ denotes the number of grey levels of this image (typically $G = 256$). These $G$ classes define a partition of the reference image, but do not necessarily correspond to connected components in this image. The resulting spatial partition is projected on the image to be registered, yielding the same partition of this second image. The expected values $\mu_g, g = 1, \ldots, G$, and the standard deviations $\sigma_g, g = 1, \ldots, G$ of each segmented region in the second image are then computed. If the two images are correctly registered, Woods assumes that the normalized variance $\sigma_g/\mu_g$ is minimum over the entire image [5]. The following *inter-image uniformity cost function* is thus defined:

$$E(I_{\text{ref}}(\cdot), I_{\text{reg}}(T_\Theta(\cdot))) = \sum_{g=1}^{G} \frac{N_g \sigma_g(T_\Theta(\cdot))}{N \mu_g(T_\Theta(\cdot))}, \tag{4}$$

where

$$\sigma_g(T_\Theta(\cdot)) = \sqrt{\sum_{x|I_{\text{ref}}(x)=g} [I_{\text{reg}}(T_\Theta(x)) - \mu_g(T_\Theta(\cdot))]^2} \tag{5}$$

and

$$\mu_g(T_\Theta(\cdot)) = \frac{1}{N_g} \sum_{x|I_{\text{ref}}(x)=g} I_{\text{reg}}(T_\Theta(x)). \tag{6}$$

In Eq. (4), $N$ represents the number of voxels in the images and $N_g$ stands for the population of voxels having the value $g$ in the reference image. This criterion has been devised for multimodal image registration. It may of course also be used for single modal image registration, although it is generally not as accurate as the least squares metric (as will be seen in our experiments).

As pointed out by Woods [5], the inter-image uniformity hypothesis may only define a crude approximation in some cases. This is particularly true when the multimodal image pair is used for the complementary and non-redundant information it provides. The dissimilarities (i.e. innovation) carried by the first image with respect to the second one are not taken into account in the inter-image uniformity cost function, leading to registration errors which, even small, may affect the accurate detection of inter-image changes [4] or the fusion of multimodal information. If the inter-image uniformity hypothesis is well verified, the histogram of the region in the registered image $I_{\text{reg}}(T_\Theta(\cdot))$, corresponding to a given grey-level class $g$ in the reference image $I_{\text{ref}}(\cdot)$, is typically peak-shaped, as represented in Fig. 1a. In practice, the typical histograms computed on real-world registered image pairs differ often significantly from this ideal shape, as can be seen in Fig. 1b, which has been obtained on an accurately registered MR/SPECT image pair. Since the SPECT image carries non-redundant functional information, many outliers occur and the histogram diverges from the ideal peak. In such cases, the computation of $\mu_g$ and $\sigma_g$ may be severely affected by the outlying data. This discrepancy with respect to the inter-image uniformity hypothesis is also readily visible on the joint histogram of the registered MR/SPECT image pair, represented in Fig. 2, which shows that the joint information is scattered over the different grey levels, with many outliers. Robust similarity metrics enable to cope efficiently with this problem, as explained in Section 3.

For comparison purposes, we will also consider a criterion based on the maximization of the mutual information proposed recently and independently [7,6]. This criterion is based on the same partitioning as in Eq. (4). The assumption is that the the mutual information $\mathcal{I}$ is maximum when the two images are correctly registered, yielding the following *mutual information cost function* [7,6]:

$$\begin{aligned} E(I_{\text{ref}}(\cdot), I_{\text{reg}}(T_\Theta(\cdot))) &= -\mathcal{I}(I_{\text{ref}}(\cdot), I_{\text{reg}}(T_\Theta(\cdot))) \\ &= -\sum_{g=1}^{G} \sum_{k=1}^{K} p(g,k) \log \frac{p(g,k)}{p(g)p(k)}, \end{aligned} \tag{7}$$

where $G$ and $K$ stand for the number of grey levels of $I_{\text{ref}}$ and $I_{\text{reg}}$. The joint probabilities $p(g,k)$ are the elements of the cooccurrence matrix of $I_{\text{ref}}(\cdot)$ and $I_{\text{reg}}(T_\Theta(.))$ and $p(g)$ and $p(k)$ are the marginal probabilities of $I_{\text{ref}}(\cdot)$ and $I_{\text{reg}}(T_\Theta(\cdot))$ respectively, both computed from the normalized histograms of the two images.

This criterion has been recognized, in several recent studies [8], as yielding the best results in multimodal medical image registration. It will be compared to our robust multimodal registration criterion in Section 4.

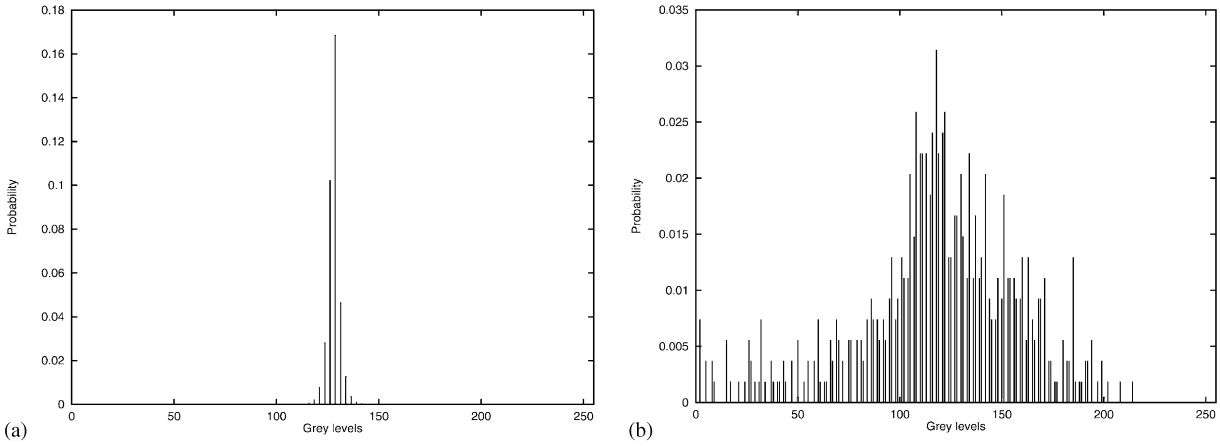


Fig. 1. (a) The theoretical histogram of the voxels in the registered image whose counterpart in the reference image have the same grey level $g$. The basic assumption of the inter image uniformity criterion is that, after registration, all the voxels in the reference image with the same grey level $g$ are represented by a constant grey level in the registered image (the peak here). (b) A typical example of an experimental histogram computed on a registered MRI/SPECT pair (the images are shown in Fig 9). Notice the amount of outliers and the discrepancy with respect to the inter-image uniformity hypothesis.

## 3. Robust similarity metrics-based registration

### 3.1. Robust similarity measures

Standard similarity-based approaches do not model the information differences between images in a single or multimodal pair and, as a consequence, are not robust with respect to them. It is well known that least squares are sensitive to gross differences between images due to non-Gaussian "events" [4] or "outliers". Outliers contribute too much to the least-squares solution since outlying points are assigned a high weight by the quadratic estimator (3). This remark also holds for the inter-image uniformity cost function (4), which is based on standard image statistics (i.e., mean values and variances) and assumes a strict agreement between uniform regions in the multimodal pair. When a significant amount of outliers is present in the images to be registered, inaccurate registrations or even misregistrations may be obtained. To increase robustness, the cost function must thus be forgiving about outlying measurements.

Robust estimators have become popular in computer vision applications because they have proven effective in tolerating gross outliers in the data [17,18]. A review on robust estimators in computer vision has been presented by Meer [17]. A collection of non linear robust estimators, including least median of squares, least-trimmed squares, M-estimators, Hough transforms, RANSAC and MINPRAN algorithms are presented by Black [19]. The robustness of these estimators to situations in which mixture of data from multiple (coherent) structures plus gross outliers are to be handled is studied in depth by Stewart [18] where it is shown that the estimated parameters may be heavily skewed in such situations.

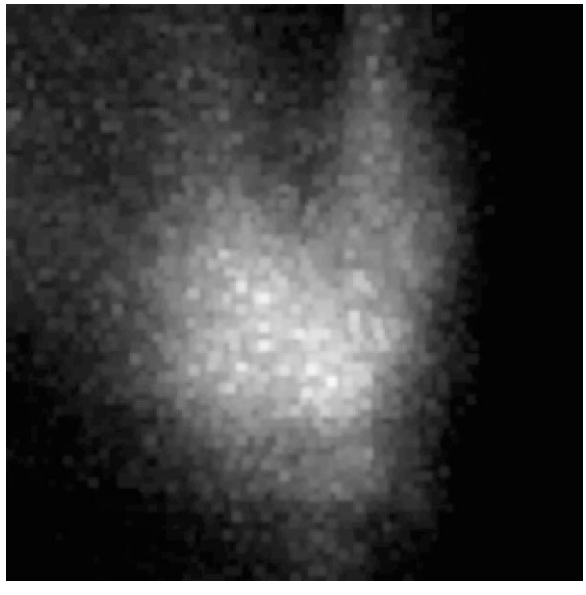

Fig. 2. The joint histogram of the registered MRI/SPECT pair shown in Fig. 9. The MRI grey levels are represented along the horizontal axis while the SPECT image grey levels are represented vertically.

A standard performance measure for a robust estimator is its breakdown point. The breakdown point is the largest fraction of data that can be arbitrarily bad and will not cause the solution to be arbitrarily bad. The least

median of squares regression [16], (used by Alexander et al. [15] for feature-based single-modal image registration), relies on the minimization of the median of the squared residuals. The resulting estimator can resist to the effect of nearly 50% of contamination in the data. In the special case of simple regression, it corresponds to finding the narrowest strip covering half of the observations. The MINPRAN algorithm [18] has also a breakdown point of 50% and relies on random data sampling. These estimators have high breakdown points but also yield a high computational load, since they are based on random data sampling and sorting. Another class of estimators, the M-estimators [20], that have attractive properties (i.e., satisfactory breakdown points and moderate computational cost), have been extensively used in computer vision [19,17]. This class of robust estimators reduces the optimization problem to a simple, low cost, weighted least-squares problem [19,17]. They have a theoretical breakdown point of $1/(p+1)$, where $p$ is the number of parameters to fit [17]. In practice, it has been observed, in a similar low-dimensional estimation problem [22], that this family of robust estimators can tolerate roughly up to 35–45% of the data as outliers. Thus, M-estimators provide a good compromise between computational complexity and outlier rejection capacity.

A robust M-estimator of parameters $\Theta$ is obtained by introducing a robust error norm ("loss" function) $\rho$ in the similarity metrics (3) and (4) [17]:

For the single modality case, we define the *robust least-squares cost function*:

$$E(I_{\mathrm{ref}}(\cdot), I_{\mathrm{reg}}(T_\Theta(\cdot))) = \sum_x \rho\{I_{\mathrm{ref}}(x) - I_{\mathrm{reg}}(T_\Theta(x)), C\}, \quad (8)$$

where $C$ is a scale (noise) parameter and $\rho$ is a non-quadratic error norm (penalty function) associated with the M-estimator. Variants of this robust cost function have been used with success in image processing and computer vision problems such as surface reconstruction [19], image segmentation, computed imaging [23], optical flow measurement [24,21] etc.

For multimodal images, we define a novel *robust inter-image uniformity cost function*:

$$E(I_{\mathrm{ref}}(\cdot), I_{\mathrm{reg}}(T_\Theta(\cdot))) = \sum_{g=1}^{G} \frac{N_g}{N} \tilde{\sigma}_g(T_\Theta(\cdot)), \quad (9)$$

where

$$\tilde{\sigma}_g(T_\Theta(\cdot)) = \sqrt{\sum_{x|I_{\mathrm{ref}}}(x) = g \rho\{I_{\mathrm{reg}}(T_\Theta(x)) - \tilde{\mu}_g(T_\Theta(\cdot)), C\}} \quad (10)$$

and

$$\tilde{\mu}_g(T_\Theta(\cdot)) = \arg\min_{\mu_g} \frac{1}{N_g} \sum_{x|I_{\mathrm{ref}}(\vec{x}) = g} \rho\{I_{\mathrm{reg}}(T_\Theta(x)) - \mu_g, C\}. \quad (11)$$

Let us notice that the non-robust cost functions (3) and (4) correspond to the special case $\rho(x,C) = x^2$ (for defining Eq. (9) we consider a non-normalized version of Eq. (4), which has shown more efficient than the original Woods' criterion). In the single-modal case (8), the cost function is simply defined as a robust error norm of the residual differences between the two registered images. In the multimodal case (9), a "robust variance" $\tilde{\sigma}_g$ is computed for each region of the image to be registered, according to Eq. (10). This robust variance does not take into account outliers in the registered image, owing to the robust error norm $\rho$. A robust estimation of the expected value $\tilde{\mu}_g$ (11) of the region is simultaneously computed by the same M-estimator. Let us emphasize that both the expected value and the variance of each region have to be computed using a robust estimator to get satisfactory results.

For the experiments presented in this paper we have tested two "hard redescending" M-estimators [18] (namely the truncated quadratic $\rho$-function [19] and the Tukey "biweight" $\rho$-function), as well as a "soft redescending" estimator (the Geman–McClure $\rho$-function [19]). Hard redescending estimators have finite rejection points. Their influence function, $\Psi(x) = \mathrm{d}\rho(x)/\mathrm{d}x$, which characterizes the influence of the residuals, verifies $\Psi(x) = 0$ for $|x| > c$. Soft redescending estimators do not have a finite rejection point but force $\Psi(x) \to 0$ as $|x| \to \infty$. We privileged the Geman–McClure estimator because it required less calculations for almost the same accuracy as the Tukey "biweight" estimator. It showed less sensitive to initialization than the truncated quadratic.

The Geman–McClure $\rho$-function (Fig. 3) [19] is defined by

$$\rho(x, C) = \frac{x^2}{C^2 + x^2}.$$

As can be seen in Fig. 3, as the magnitude of the residuals increases and grows beyond a point, its influence on the solution begins to decrease and the value of $\rho(x)$ approaches a constant. The scaling parameter $C$ affects the point at which the influence of outliers begins to decrease. For the error norm used in our experiments, points $x$ for which

$$|I_{\mathrm{ref}}(T_\Theta(x)) - I_{\mathrm{reg}}(x)| \geqslant \frac{C}{\sqrt{3}}$$

can be viewed as outliers, as the outliers rejection begins where $\partial^2\rho/\partial x^2 = 0$.

The calculation of the registration parameters $\Theta$ involves the minimization of the non-linear cost functions (8) or (9) which depend on the scale parameter $C$. A good strategy [18] consists in starting the optimization procedure with a high value for $C$. The value of $C$ decreases during the minimization process following the formula

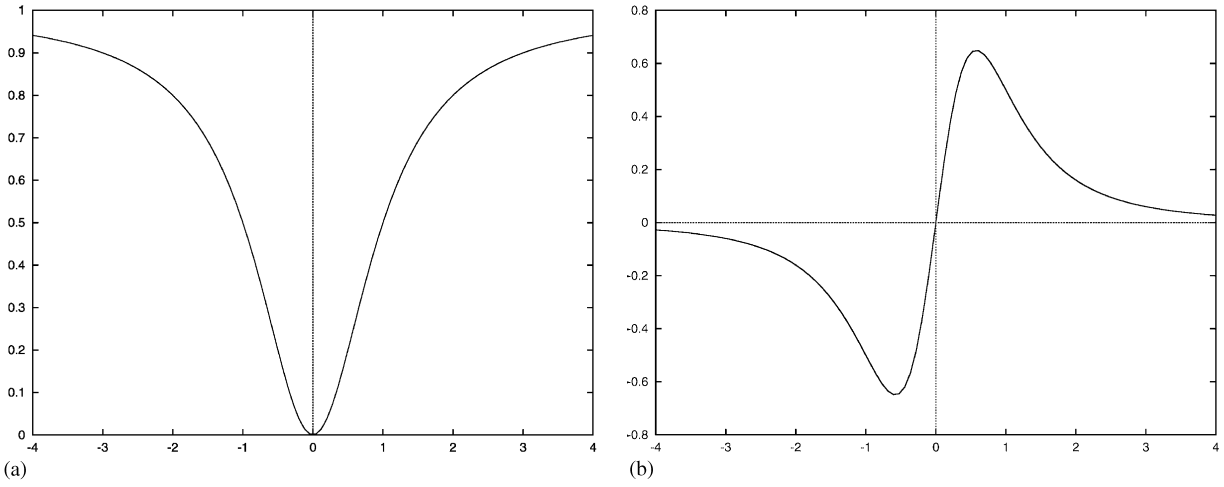


Fig. 3. The Geman-McClure robust estimator $\rho(x)$ (a) and its influence function (b).

$C = \alpha.C$ with $0.8 < \alpha < 1$ until $C$ reaches a predefined value. The effect of this procedure is that initially no data are rejected as outliers and a first, crude solution is obtained. During the following optimization steps the influence of the outliers is gradually reduced by decreasing $C$, leading to a reliable estimation of the rigid transformation parameters, which is robust to gross image differences. In other experiments we have also estimated $C$, as the noise variance computed on homogeneous regions of the original images (other statistical methods for estimating $C$ from the data may be found in the work of Stewart [18]). These different strategies provided us with almost the same qualitative results.

### 3.2. The multiresolution stochastic registration algorithm

The non-robust estimators considered previously are highly non-linear, involving non-convex cost functions having multiple local minima [25]. In most image registration methods based on the minimization of a cost function, deterministic optimization algorithms are applied. They are known to be very sensitive to local minima, unless they are initialized close to the optimal solution.

In order to increase robustness to local minima of the similarity function and to obtain data driven registrations, the parameter space has been discretized and a fast stochastic optimization algorithm has been applied. Stochastic optimization, based on random sampling, is far less sensitive to local minima, yielding better, often close to the optimal solutions [18]. The optimization technique used in our implementation is based on the Gibbs sampler [26]. A high value is adopted for the initial temperature in a simulated annealing procedure and a fast exponentially decreasing temperature schedule is considered instead of the optimal logarithmic descent [26]. The solution obtained after a given number of steps is further refined by a deterministic extension of the above algorithm, known as iterated conditional modes (ICM) [27]. ICM is a deterministic Gauss–Seidel like algorithm, that only accepts configurations decreasing the cost function. It has fast convergence properties and local minima are not a problem, since the first stochastic optimization step provides a good initialization.

The optimization algorithm is applied on a sequence of multiresolution grids, using a standard top-down approach starting from the coarsest resolution level [21,28]. The solution obtained at a given resolution level is interpolated and forwarded to the next, finer resolution. The algorithm first carries out the calculations for every 81st (16th) voxel (pixel) in the 3D (2D) images. After the algorithm has converged, the resulting registration parameters represent the initial estimate for the next level, where every 27th (8th) voxel is processed, then every 9th (4th), every 3rd (2nd) and finally every voxel (pixel) in the image. The search space and the visited configurations are reduced while the resolution increases in order to gradually fine tune the solutions obtained on the coarser resolution levels. The first grids generally provide a good approximation of the final solution. Multigrid matching is usually motivated by the significant computational gain obtained in the registration. As noticed by several authors [25], multigrid algorithms are also far less sensitive to local minima in the cost function than single-resolution optimization schemes. It has indeed been conjectured that multigrid analysis may, to a certain extent, smooth the "landscape" of the objective function to minimize. This yields fast convergence towards good solutions [25].

Let us finally notice that a large number of interpolations are involved in the registration process. The accu-

racy of the rotation and translation parameter estimates is directly related to the accuracy of the underlying interpolation model. Simple approaches such as the nearest-neighbour interpolation are commonly used because they are fast and simple to implement, though they produce images with noticeable artifacts. More satisfactory results can be obtained by small-kernel cubic convolution techniques, trilinear (bilinear) interpolation, bicubic spline interpolation or convolution-based interpolation. According to the sampling theory, optimal results are obtained using sinus cardinal interpolation, but at the expense of a high computational cost. As a compromise, we have used a fast nearest-neighbour interpolation technique in the first optimization steps. At the end of the algorithm (i.e. on the finest resolution grid), the registration parameters are refined using a trilinear (or bilinear) interpolation that preserves the quality of the image to be registered. This technique has shown fast and accurate.

The different steps of the multigrid registration algorithm are thus the following:

- Reduction of the grey levels of the reference image (usually to 256).
- For every resolution level:

  ○ Registration of the volumes of interest by fast stochastic optimization of the robust similarity measure (Fig. 4).
  ○ Fine tuning of the solution using a deterministic optimization algorithm (Fig. 5).
  ○ Interpolation of the 3D translation and rotation parameters to be forwarded to the next (finer) resolution level.

For the registration of two $N \times N \times N$ images, the above described algorithm is $O(LMN^3)$, where $M$ is the number of discrete elements of the parameter space and $L$ stands for the number of reductions of the search space.

## 4. Experimental results

Registration experiments were performed with both 2D and 3D images. The following similarity measures have been implemented and compared:

- the standard least-squares (LS) similarity measure Eq. (3));
- the inter-image uniformity (IU) criterion devised by Woods et al. [5] (Eq. (4));
- the mutual information (MI) criterion proposed in [6,7] (Eq. (7));
- the robust least-squares (RLS) similarity metrics (Eq. (8));
- the robust inter-image uniformity (RIU) criterion (Eq. (9)).

- SIMULATED ANNEALING $(\Theta_0, T_0, c, E, max)$
  - $\Theta_0$ initial parameters $(t_x, t_y, t_z, \hat{\theta}_x, \hat{\theta}_y, \hat{\theta}_z)$
  - $T_0$ initial temperature
  - $c$ cooling parameter
  - $E$ energy function
  - $max$ maximum number of iterations
  - $T \leftarrow T_0$ ; $k \leftarrow 0$ (counter) ; $\Theta \leftarrow \Theta_0$ ;
  - **while** $k \leq max$ **do**:
    - randomly chose an element $\Theta_k(i)$ of $\Theta_k$ at iteration $k$ with a uniform probability distribution ;
    - construct $M$ configurations different from $\Theta_k$ only by the element $\Theta_k(i)$ ;
    - configuration $\Theta_k = S$ is accepted with a probability:

$$P(\Theta = S|\Theta_{j|j\neq k}) = \frac{\exp\ -\frac{E(\Theta_1,\ldots,\Theta_k=S,\ldots\Theta_M)}{T_k}}{\sum_{\Theta_k}\exp\ -\frac{E(\Theta_1,\ldots,\Theta_k,\ldots\Theta_M)}{T_k}}$$

    - $T_{k+1} \leftarrow c \times T_k$
    - $k \leftarrow k+1$
  - **end do**

Fig. 4. The version of simulated annealing implemented in our registration experiments.

- ICM $(\Theta_0, E, max)$
  - $\Theta_0$ initial parameters $(t_x, t_y, t_z, \hat{\theta}_x, \hat{\theta}_y, \hat{\theta}_z)$
  - $E$ energy function
  - $max$ maximum number of iterations
  - all parameters are declared unvisited ;
  - $\Theta \leftarrow \Theta_0$ ; $k \leftarrow 0$ (counter) ;
  - **while** $k \leq max$ **do**:
    - **while** there are unvisited parameters **do**:
      - randomly chose un element $\Theta_k(i)$ of $\Theta_k$ at iteration $k$ ;
      - construct several configurations different from $\Theta_k$ only by the element $\Theta_k(i)$ ;
      - keep the configuration giving the minimum energy;
      - declare parameter $\Theta(i)$ visited
    - **end do**
  - reduce parameter search space
  - declare all parameters unvisited
  - $k \leftarrow k+1$
  - **end do**

Fig. 5. The iterated conditional modes (ICM) algorithm implemented in our registration experiments.

LS and RLS may only be applied to single-modal image registration, whereas the other methods (IU, RIU, MI) have been tested both in single and multimodal registration problems. Three representative case studies

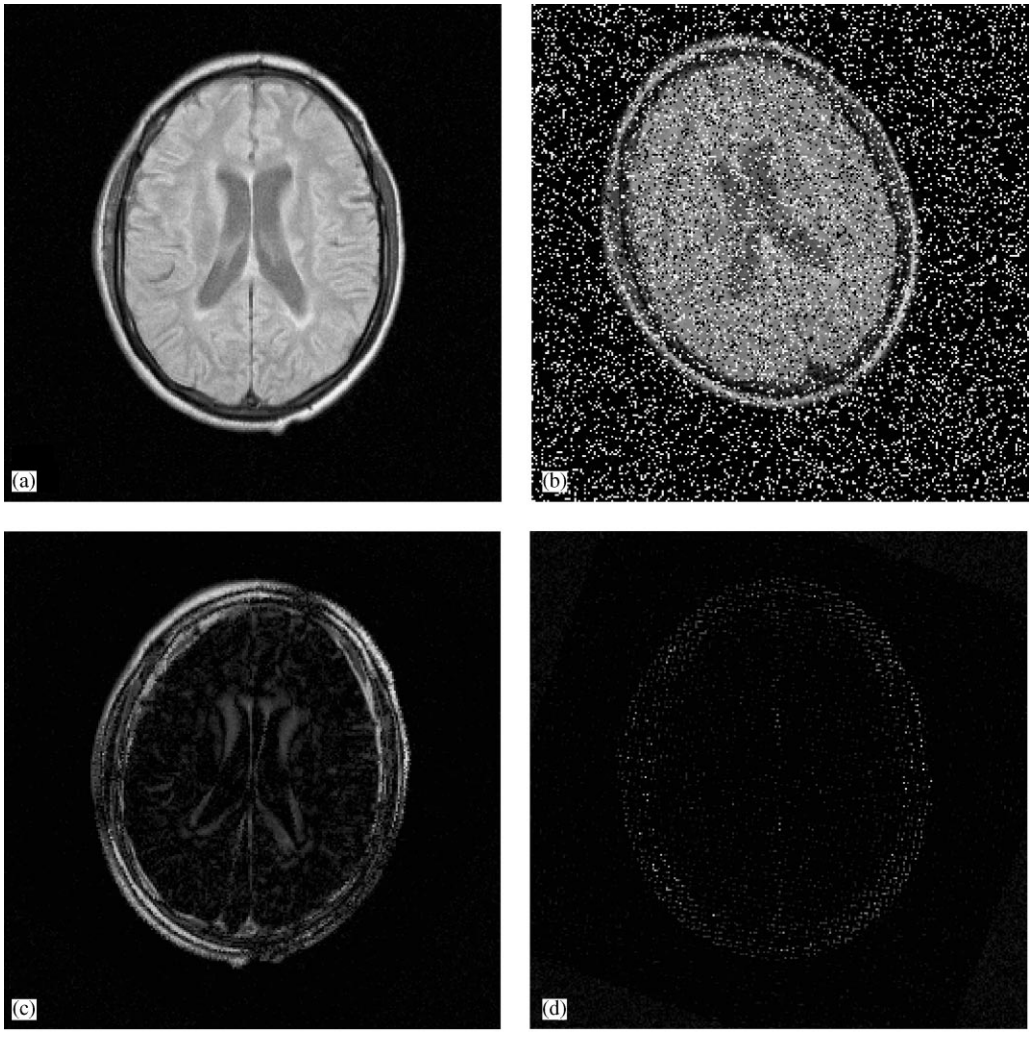


Fig. 6. Robust registration of MR images. (a) reference image; (b) image in (a) rotated by 20°, translated by 10 pixels along the $x$-axis, 10 pixels along the $y$-axis and corrupted at 25% with salt and pepper noise with large magnitude; (c) difference between the (noise free) registered image and the image in (a) (LS similarity metric); (d) difference between the (noise free) registered image and the image in (a) (robust RLS similarity metric).

have been considered: the registration of single modal (MRI/MRI) and multimodal (MRI/SPECT) 3D medical images showing gross outliers or lesion evolution, the matching of multispectral (visible/IR) remotely sensed images showing large overcast areas and the registration of intensity images to their range data counterpart.

Computation and display were performed on a Hewlett-Packard HP 9000/C200 workstation by using a 2D–3D image analysis software (MEDIMAX) developed at IPB. This software, running under Unix, is developed in C language and uses the standard graphics interface X11/R5 and the Motif windows manager. All registrations techniques presented in this paper were implemented under this software environment and are easily available to users. The software is available on the IPB web server (http://alsace.u-strasbg.fr).

The results presented in the following tables are reported in terms of translation (voxels) and rotation angles (deg). It is commonly accepted that evaluation of translations and rotations is not straightforward as these two measures interact. Another choice would be to define landmarks in the images and evaluate the registration error on them. However, as manual definition of landmarks could have introduced additional errors we prefered to express our results in terms of voxels and angles. In the remainder of the paper, the term "subvoxel error" stands for errors that are less than 1 voxel in translation and 1° in rotation.

### 4.1. Single-modal image registration

#### 4.1.1. Medical images

A first class of experiments consisted in applying a known rigid transformation (3D translation and rotation) to a set of MRI volumes to create a second image set. Twenty-five percent of the transformed images was then corrupted by salt and pepper noise, to simulate gross outliers (see Fig. 6a and b). For each method, the estimated registration parameters were compared to the true ones to determine the accuracy of the registration. Statistics on the registration errors were computed on a set of 20 different registrations problems, involving translation parameters between $-20$ and $+20$ voxels and rotations between $-30$ and $+30^{\circ}$. Let us notice that large rotations are generally difficult to handle with standard, deterministic approaches (in which initializations close to the desired solution are necessary). This is not the case of the stochastic sampling algorithm used here.

As we can see in Table 1, the robust algorithms achieved subvoxel registration errors while the non-robust (LS and IU) techniques failed. The MI method, the best-method referenced at the present time [8], also achieved subvoxel registration but its performances are slightly inferior to the results obtained by the RLS technique.

Fig. 6c shows an example where the standard method (LS) failed to correctly register the MR slices shown in Fig. 6a and b, but where the RLS achieved accurate matching by discarding outliers. The difference in accuracy is readily visible on the magnified registration errors shown in Fig. 6c and d, corresponding to the residual squared image difference after registration.

We also show in Fig. 7 an example of the application of the RLS algorithm to the detection of changes in a set of MRI slices of a multiple sclerosis patient, acquired at different dates. Fig. 7 illustrates a case on which small differences due to lesion evolution, which were not well distinguished previously due to misalignment by the standard LS similarity metric (Fig. 7c), are now clearly identified by simple image subtraction (Fig. 7d). This result has been validated by an expert physician from IPB.

#### 4.1.2. Remotely sensed images

Two images of France, in the infra-red band of NOAA (Fig. 8a and b), acquired at different dates and showing large overcast areas, have been manually registered to establish ground truth. One of the images has been transformed using different 2D rotation and translation parameters and the registration algorithms were applied. This case, contrary to the example considered previously (Section 4.1.1), does not correspond to a corruption of the data by gross outliers, but to the presence of multiple coherent structures (i.e. ground and clouds) in the data. Mixture of data from multiple (coherent) structures introduces a significant bias in all robust estimators, as shown in a recent study by Stewart [18]. The performances of the robust methods are affected by this bias, as can be seen in Table 2 in which the different approaches are compared. The registrations are not as accurate as in the previous case, although a subpixel accuracy is reached, and the difference between methods is less pronounced. The robust methods produce nevertheless the best results and compare favourably to the MI approach.

Fig. 8 illustrates the contribution of the RLS metric with respect to a non-robust LS metric, in the registration of the original infra-red image pair. The original images show a misregistration of about three pixels. Clouds in the second image lead the LS technique to a slight misalignment (Fig. 8c) while the RLS measure provides a more accurate registration (Fig. 8d). The difference is readily visible along the southwest coast of France. The registration errors presented in Fig. 8c and d are obtained by subtraction of the registered image from the reference image in Fig. 8a, followed by contrast modifications for visualization purpose.

### 4.2. Multimodal registration

#### 4.2.1. Medical images

To evaluate the ability of the robust similarity metrics to handle multimodal image pairs, a 3D SPECT image volume has been manually registered to its corresponding MRI volume with the aid of an expert physician from IPB. The manually registered SPECT volume was then transformed using the same 3D translation and rotation parameters as in the previously described experiments (Section 4.1.1). To simulate outliers, 25% of the SPECT image was corrupted by salt and pepper noise. The robust inter-image uniformity technique RIU has been compared to the inter-image uniformity similarity function IU [5] and to the mutual information MI criterion [6,7]. Table 3 shows the robustness of the different similarity measures to gross outliers. The error for the RIU method is about 1 voxel for the translation parameters and $1^{\circ}$ for the Euler rotation angles. This is significantly more accurate than the IU approach. The proposed robust similarity metric also compares favourably to the MI criterion which yields registrations that are better than the IU criterion but are generally below RIU.

Figs. 9 and 10 show a real example of a patient brain SPECT volume registered with respect to its MRI counterpart by the different algorithms. Robustness to the presence of non-brain structures has been examined in this case. The similarity metrics (IU, MI, RIU) are applied to MRI/SPECT registration without prior removal of skull and scalp from the MR volumes. This preprocessing is customary when registering brain image volumes [5], but often requires manual human interaction.

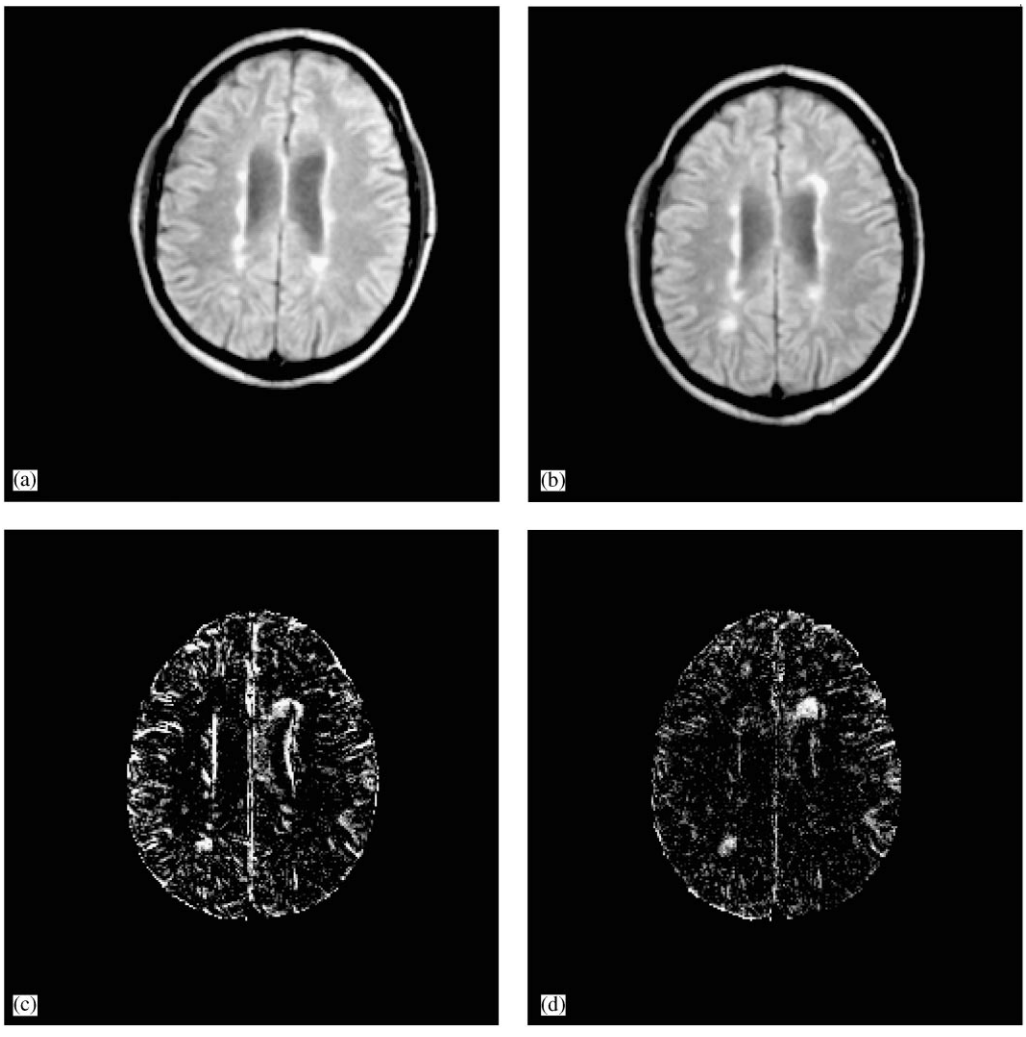


Fig. 7. Change detection in a MRI image sequence. (a) multiple sclerosis patient MR image; (b) image of the same patient acquired several months later and showing lesion evolution; (c) difference between the registered image and the image in (a) (LS similarity metric); (d) difference between the registered image and the image in (a) (robust RLS similarity metric).

Our results confirm that the IU criterion is trapped by local minima [15], since it considers outliers (nonbrain structures) as a part of the data (Fig. 9b). On the other hand, mutual information (Fig. 10a) and M-estimators (Fig. 10b) provide approximately similar results with a relatively good accuracy. The accuracy of the robust registration has been evaluated by visual inspection and has been considered satisfactory by an expert.

*4.2.2. Remotely sensed images*

We consider again the case of multispectral remotely sensed images, presenting coherent data corruption due to large overcast areas. Two images, one in the visible and one in the infrared band of NOAA, acquired at different dates (Fig. 11a and b) were manually registered to establish ground truth. One of the images has been transformed using different rotation and translation parameters and the multimodality registration algorithms were applied. The performances of the different methods are summarized in Table 4. As expected the robust RIU criterion provides registrations that are significantly more accurate than the non-robust IU technique. The difference between the tested similarity metrics is, however, not as pronounced as for the medical images registration problem (in which gross outliers were considered). This may again be explained by the bias introduced by the mixture of data from multiple coherent structures on the robust estimation [18]. In this particular case, the mutual information MI criterion yields, in the average, the best results. Let us, however, notice that

Table 1
Single-modal registration of 3D MRI images. An MR volume was artificially transformed using 20 different rigid transformations and the images were corrupted at 25% by salt and pepper noise. The average and the standard deviation of the registration errors computed from the 20 registrations are presented for the different approaches. Translation errors are given in voxels and rotation errors in degrees

3D MRI/MRI Registration

| Approach | $\Delta t_x$ | $\Delta t_y$ | $\Delta t_z$ | $\Delta\hat{\theta}_x$ | $\Delta\hat{\theta}_y$ | $\Delta\hat{\theta}_z$ |
|---|---|---|---|---|---|---|
| LS | $2.30 \pm 1.75$ | $2.53 \pm 1.56$ | $2.77 \pm 1.83$ | $4.71 \pm 2.89$ | $5.33 \pm 3.40$ | $5.05 \pm 3.51$ |
| IU | $1.49 \pm 1.40$ | $1.56 \pm 1.41$ | $1.93 \pm 1.63$ | $3.75 \pm 2.03$ | $3.65 \pm 2.54$ | $2.99 \pm 3.06$ |
| MI | $0.05 \pm 0.06$ | $0.22 \pm 0.15$ | $0.09 \pm 0.14$ | $0.35 \pm 0.35$ | $0.27 \pm 0.32$ | $0.44 \pm 0.69$ |
| RLS | $0.04 \pm 0.07$ | $0.16 \pm 0.11$ | $0.06 \pm 0.10$ | $0.41 \pm 0.21$ | $0.16 \pm 0.22$ | $0.33 \pm 0.24$ |
| RIU | $0.09 \pm 0.05$ | $0.18 \pm 0.14$ | $0.10 \pm 0.05$ | $0.22 \pm 0.34$ | $0.24 \pm 0.17$ | $0.40 \pm 0.59$ |

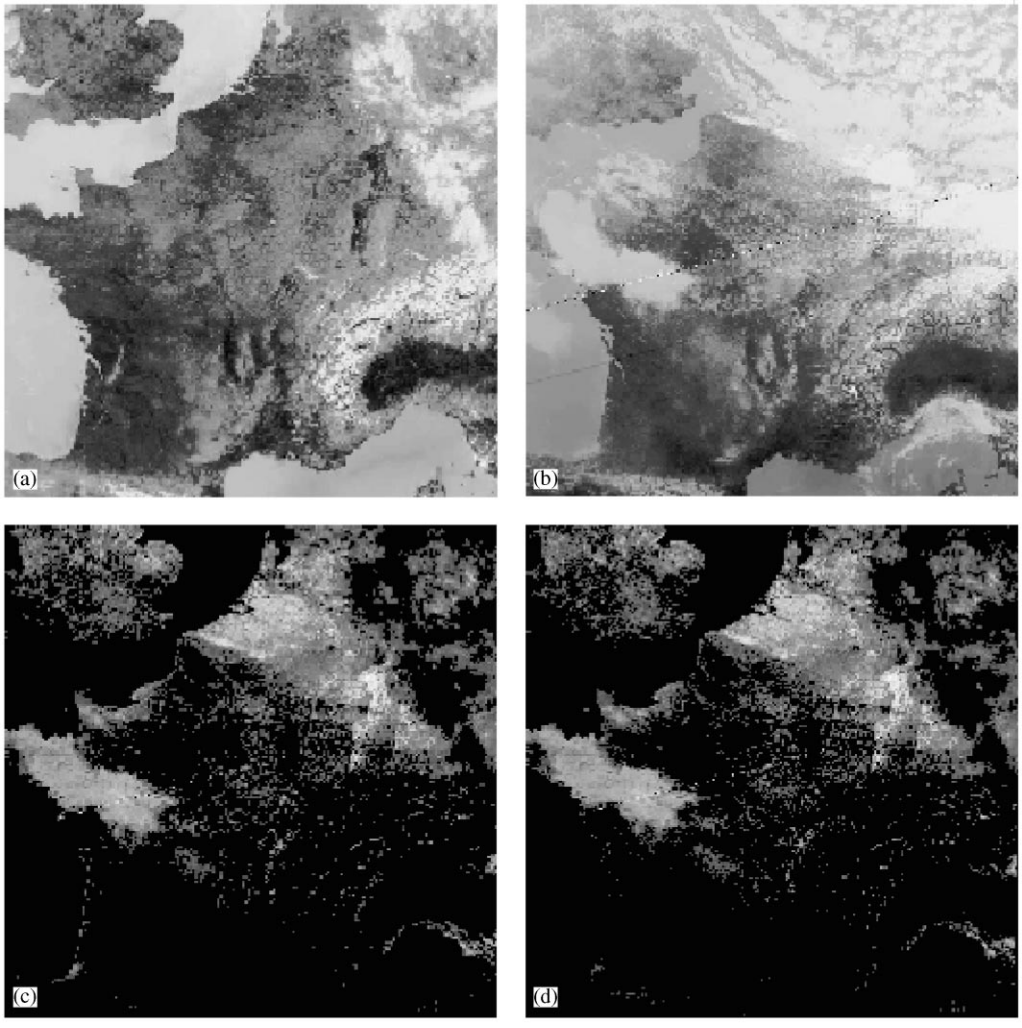


Fig. 8. Single-modal registration of remotely sensed images. (a) image of France in the infra-red band of NOAA (02/10/97); (b) image of France in the infra-red band of NOAA (02/05/97); (c) registration error (LS similarity metric); (d) registration error (robust RLS similarity metric).

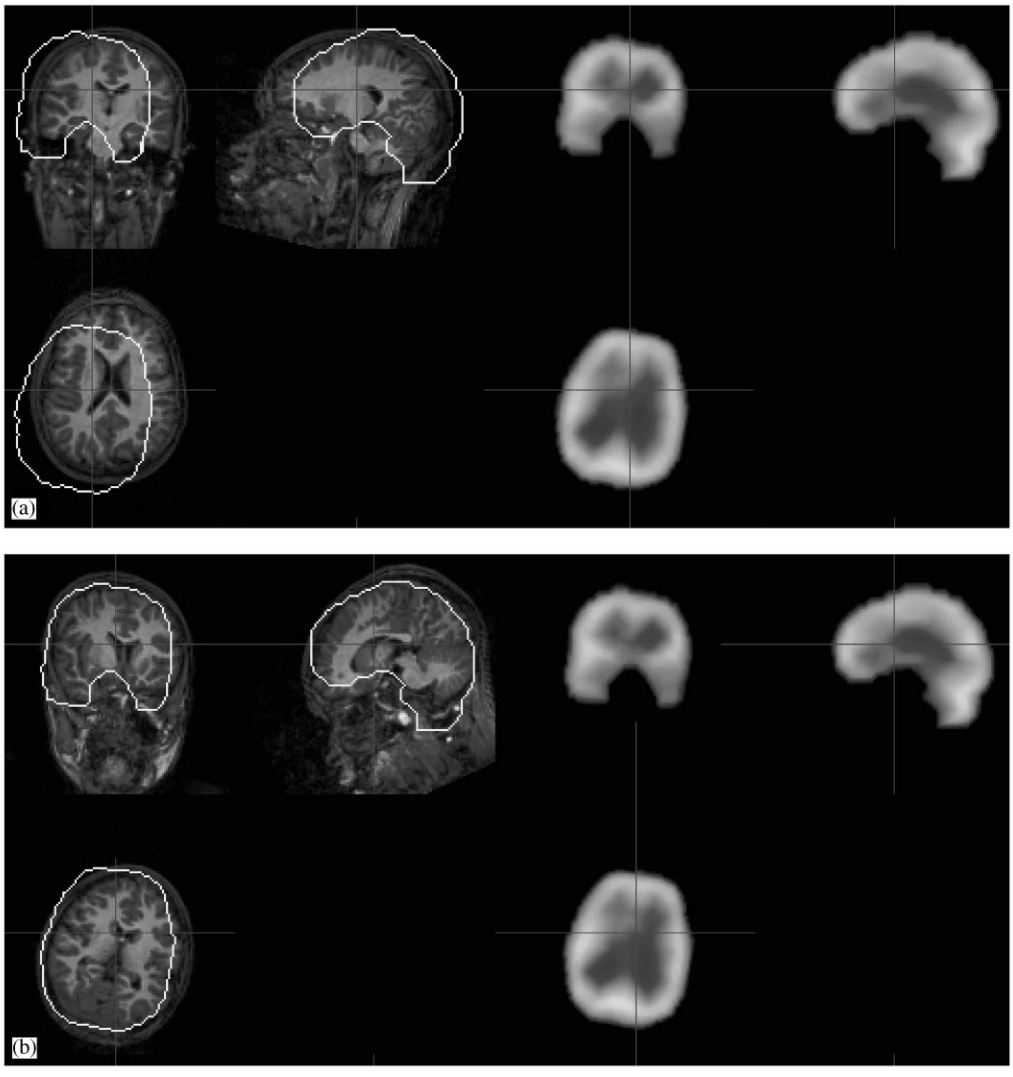


Fig. 9. MRI/SPECT volume registration of the brain (non-brain structures have not been removed). The SPECT and MRI volumes with the SPECT contours superimposed on the MRI are shown (by multiplanar visualization). (a) MRI/SPECT volumes before registration; (b) MRI/SPECT volumes after registration (IU similarity metric).

the variance of the MI estimate is significantly higher than the variance of the robust RIU criterion (see Table 4), which tends to temper the conclusion in this case.

Fig. 11 presents the registration of the original multimodal pair. The images from the NOAA visible band (Fig. 11a) and from the NOAA infra-red band (Fig. 11b), acquired at different dates have been registered using the IU, RIU and MI approaches. In this particular case, the non robust IU metric and the MI criterion provided the same final registrations. As may be seen in Fig. 11c, the IU metric, yields a misregistration, that is visible on the error image, along the south west coast of France. This is not the case of the robust RIU similarity measure (Fig. 11d) which provides an accurate registration of this dissimilar multimodal image pair. Let us notice that the multimodal registration error shown in Fig. 11c and d is defined as the difference between the registered IR image and the IR image acquired at the same instant as the visible band reference image.

#### *4.2.3. Intensity/range images*

Finally, the proposed multimodal robust voxel similarity metric has been applied to the registration of a range image to its intensity counterpart. The synthetic stereo image in Fig. 12a is partially composed of natural

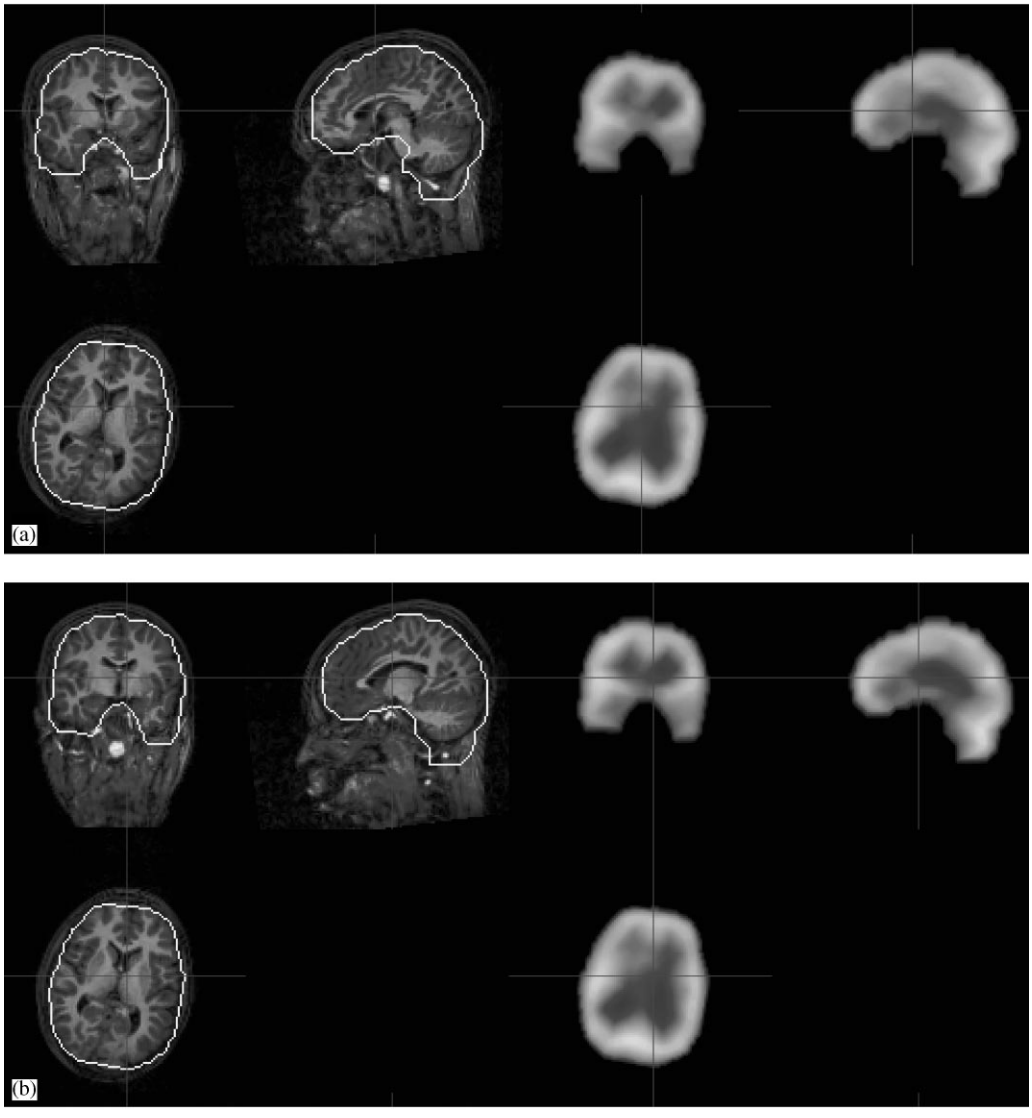


Fig. 10. MRI/SPECT volume registration of the brain (non-brain structures have not been removed). The SPECT and MRI volumes with the SPECT contours superimposed on the MRI are shown (by multiplanar visualization). (a) MRI/SPECT volumes after registration (MI similarity metric), (b) MRI/SPECT volumes after registration (RIU similarity metric).

objects. The range image is presented in Fig. 12b. The intensity image was corrupted at 25% by "salt and pepper noise" (Fig. 12c) and the range image was rotated by 15° (Fig. 12d). We have registered the rotated range image to the noisy intensity image by the inter-image uniformity measure, the maximization of the mutual information criterion and the robust version of the inter-image uniformity metric, proposed here. After registration, the registered range image was subtracted from the ground truth (Fig. 12b) and the error images are presented in Fig. 13a–c. The grey level of these error images are normalized for visualization reasons. As it can be seen, the the standard metric (Fig. 13a) is not able to provide a satisfactory registration, whereas the robust metric (Fig. 13c) provides fewer registration artefacts. The MI criterion provides better registration than the IU measure but its performances are slightly inferior to the robust metric-based method.

## 5. Discussion and conclusion

The robust similarity metrics-based registration methods described in this paper were motivated by the

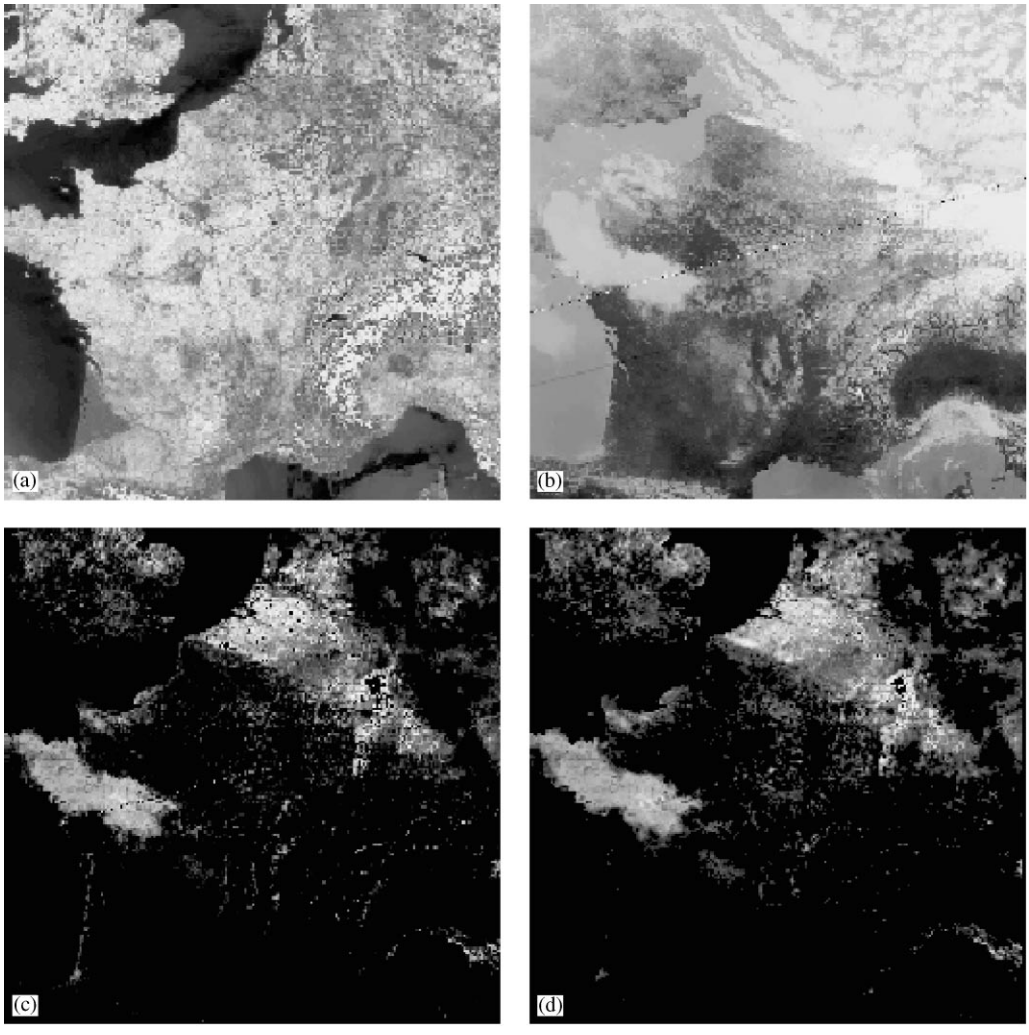


Fig. 11. Multimodal registration of visible/IR remotely sensed images. (a) image of France in the visible band of NOAA (02/10/97) (reference image); (b) image of France in the infrared band of NOAA (02/05/97); (c) Registration error (IU similarity metric); (d) registration error (robust RIU similarity metric). The registration error is defined as the difference between the registered IR image and the IR image acquired at the same instant as the visible band reference image (a).

lack, in existing approaches, of specific models for gross dissimilarities or outlying data that are often present in single and multimodal image pairs. The proposed stochastic multigrid registration algorithms have two major advantages over standard methods:

- No manual initialization near the optimal solution is required to obtain an accurate registration. Local minima, a major problem in standard image registration techniques, are avoided by the use of fast multigrid random sampling algorithms. This results in a data-driven method that requires no human interaction.
- Gross image differences are taken into account efficiently by robust M-estimators. To our knowledge, the registration of *multimodal images* showing gross dissimilarities or mixture of data from multiple coherent structures has never been evoked until now.

We have compared our robust metrics to the commonly used quadratic similarity measure, to the inter-image uniformity algorithm IU [5] and to the mutual information criterion MI [7,6].

The estimates obtained with the IU metric are significantly skewed when the images exhibit gross differences, since its cost function, based on standard image statistics, does not account for outliers. Although not stemming from robust estimation theory, the MI criterion presents an excellent robustness to outliers but its performances

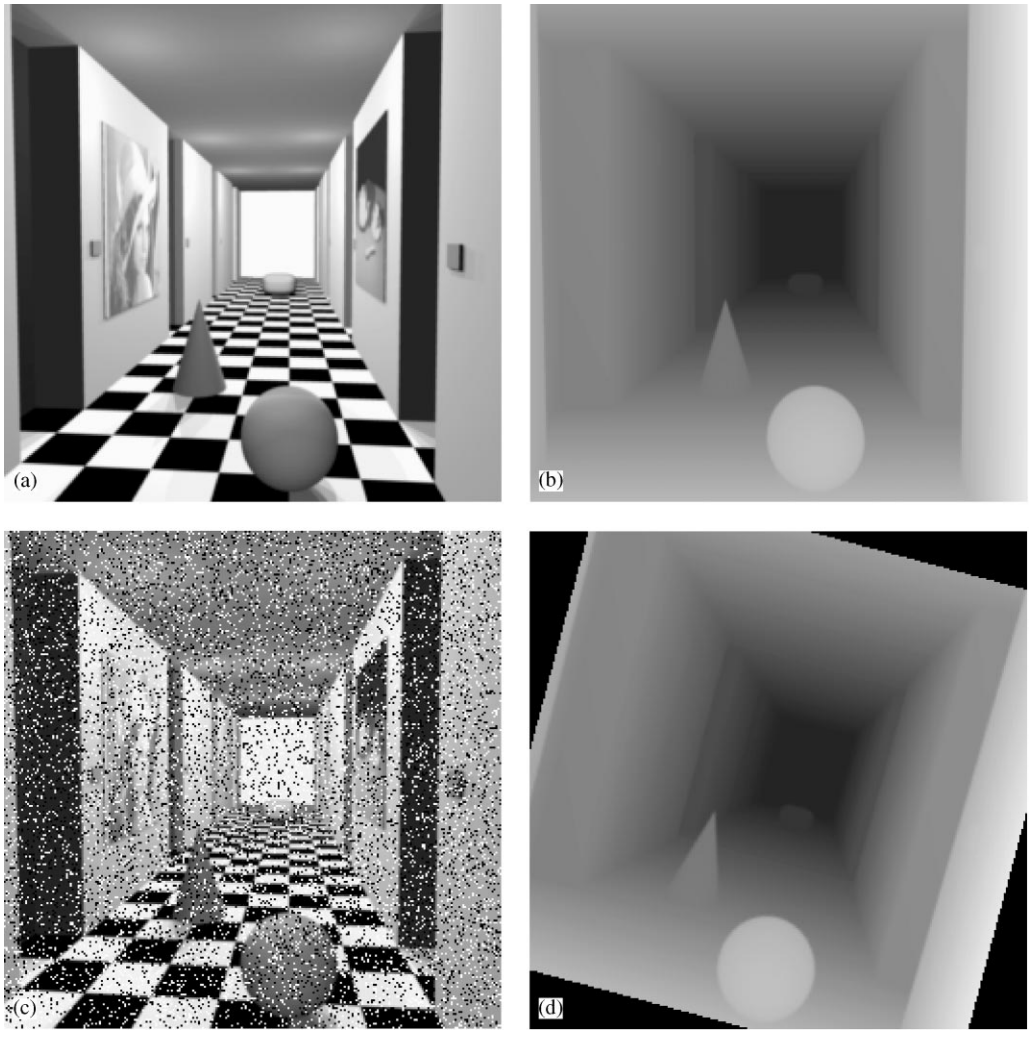


Fig. 12. Multimodal registration of intensity and range images. (a) intensity image; (b) range representation of the image in (a) (by courtesy of the Computer Vision and Pattern Recognition Group, University of Bonn, Germany); (c) image in (a) corrupted at 25% by "salt and pepper noise". (d) Image in (b) rotated by 15°.

are generally below the robust similarity metrics, when gross outliers have to be handled. The performances of MI are better on mixture of data from multiple coherent structures, while the robust estimators tend to be skewed in this case, as pointed out by Stewart [5].

Table 5 summarizes the execution times for the different registration techniques considered in our experiments. The LS and RLS techniques require approximately the same average computation times: 8 min cpu time for 3D $128 \times 128 \times 128$ images on a standard workstation. For the same data size, the IU method takes 14 min, the MI technique 16 min and the RIU method needs 24 min cpu time. In the case of 2D images ($256 \times 256$), the RIU metric requires 1 min cpu time while each of the other techniques takes approximately 30–40 s. As can be seen, the additional computational complexity introduced by the robust estimation is acceptable and these methods may thus be used with profit to improve the accuracy in many critical single or multimodal image registration problems.

The performances of the robust voxel similarity metrics proposed here may be limited if the amount of outliers present in the images is greater than the breakdown point of the estimator. Besides, images not respecting at all the image uniformity criterion (IU) cannot be processed by the proposed approach. Let us also notice that the similarity metrics examined here are not symmetric, that is if the reference image and the image to be registered are swapped the algorithm will not provide the same transformation parameters.

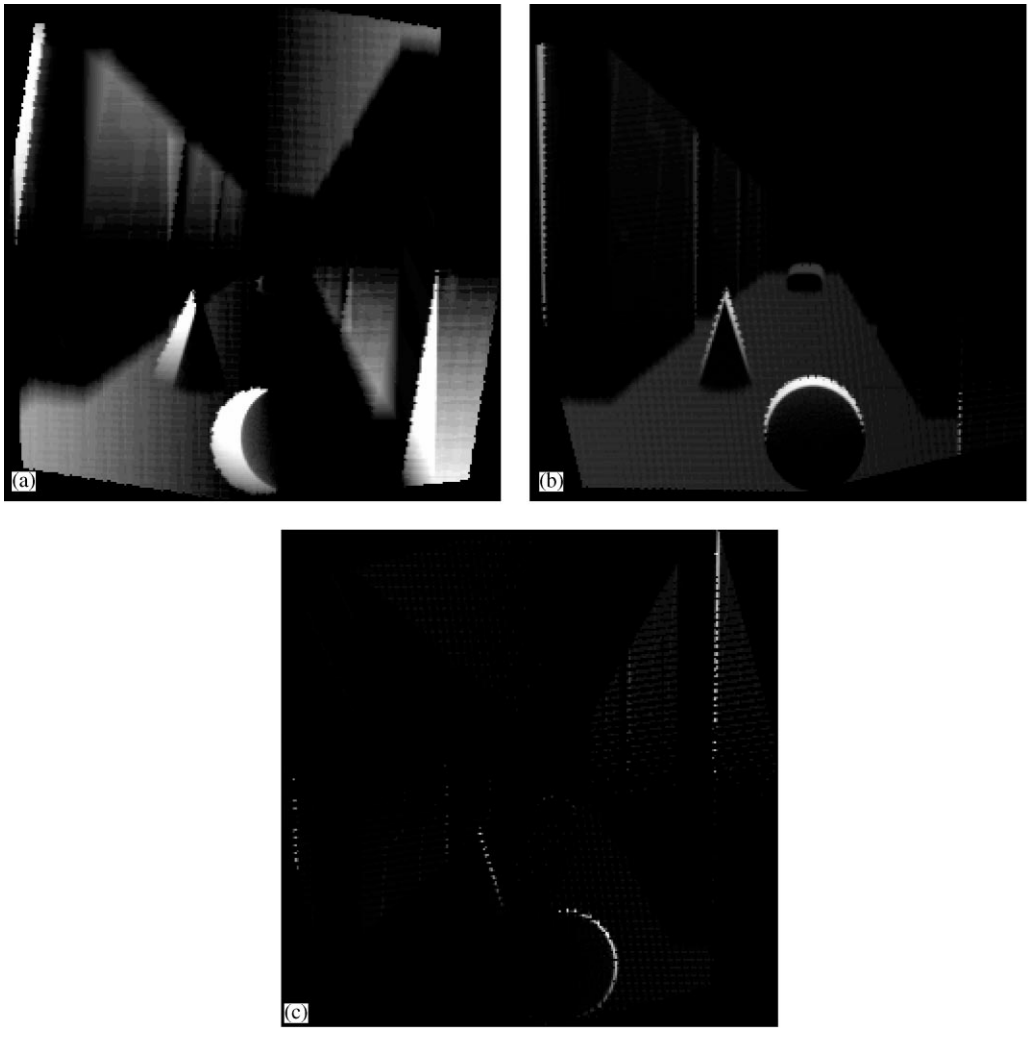


Fig. 13. Multimodal registration of the intensity and range images presented in Fig. 12c and Fig. 12d. (a) registration error for the IU metric (see text); (b) registration error for the MI metric (see text); (c) registration error for the RIU metric (see text).

Table 2
Single-modal registration of 2D remotely sensed infra-red images. Two images of the infra-red electromagnetic band of NOAA satellite acquired at different dates have been manually registered to create ground truth (the original images arepresented in Fig. 8). One of the images has undergone 20 different rigid transformations using different translation and rotation values. The average and the standard deviation of the registration errors are presented for the different approaches. Translation errors are given in pixels and rotation errors in degrees

2D IR/IR registration

| Approach | $\Delta t_x$ | $\Delta t_y$ | $\Delta\hat{\theta}$ |
|---|---|---|---|
| LS | $0.42 \pm 0.18$ | $0.31 \pm 0.41$ | $0.32 \pm 0.18$ |
| IU | $0.52 \pm 0.21$ | $0.77 \pm 0.40$ | $0.30 \pm 0.25$ |
| MI | $0.49 \pm 0.54$ | $0.63 \pm 0.25$ | $0.75 \pm 0.89$ |
| RLS | $0.36 \pm 0.10$ | $0.27 \pm 0.37$ | $0.30 \pm 0.25$ |
| RIU | $0.34 \pm 0.17$ | $0.70 \pm 0.28$ | $0.18 \pm 0.13$ |

To overcome the above-mentioned limitations, robust R-estimators may be used with a breakdown point of approximately 50% with the shortcoming of important execution times. Furthermore, an immediate perspective of our study is to define criteria deciding which image of the pair should be the reference image. Also, an improvement to the proposed multimodal registration algorithm would be to eliminate regions containing a small number of points in the joint histogram and to privilege regions of the reference image that form connected components. By these means, the algorithm would not only consider grey-level information but also spatial relations.

Finally, let us emphasize that the approach proposed in this paper is comprehensive and not limited to medical or remotely sensed images. Other potential application fields [1] such as military imaging, multisensor robot vision or the multisource analysis of artistic

Table 3
Multimodal registration of 3D MRI/SPECT images. A 3D SPECT image volume manually pre-registered by an expert to its MRI counterpart was artificially transformed using 20 different translation and rotation parameters and corrupted at 25% by salt and pepper noise. The average and the standard deviation of the registration errors are presented for the different approaches. Translation errors are given in voxels androtation errors in degrees

3D MRI/SPECT registration

| Approach | $\Delta t_x$ | $\Delta t_y$ | $\Delta t_z$ | $\Delta\hat{\theta}_x$ | $\Delta\hat{\theta}_y$ | $\Delta\hat{\theta}_z$ |
|---|---|---|---|---|---|---|
| IU | $3.85 \pm 5.59$ | $3.02 \pm 4.78$ | $4.16 \pm 4.38$ | $8.33 \pm 4.51$ | $6.23 \pm 3.52$ | $6.80 \pm 4.15$ |
| MI | $1.41 \pm 0.74$ | $1.38 \pm 1.23$ | $2.06 \pm 1.29$ | $0.94 \pm 1.58$ | $1.04 \pm 1.15$ | $1.36 \pm 0.77$ |
| RIU | $0.82 \pm 0.53$ | $0.61 \pm 0.50$ | $0.83 \pm 0.60$ | $0.21 \pm 0.48$ | $1.14 \pm 0.26$ | $0.71 \pm 0.94$ |

Table 4
Multimodal registration of 2D visible/infra-red images. Two images, one of the visible and one of the infra-red electromagnetic band of NOAA satellite acquired at different dates have been manuallyregistered to create ground truth. One of the images has undergone 20 different rigid transformations using different translation and rotation values. The average and the standard deviation of the registration errors are presented for the different approaches. Translation error are given in pixels and rotation errors in degrees

2D Visible/IR Registration

| Approach | $\Delta t_x$ | $\Delta t_y$ | $\Delta\hat{\theta}$ |
|---|---|---|---|
| IU | $1.34 \pm 0.87$ | $1.04 \pm 0.34$ | $0.34 \pm 0.27$ |
| MI | $0.40 \pm 0.68$ | $0.31 \pm 0.74$ | $0.24 \pm 0.37$ |
| RIU | $0.51 \pm 0.34$ | $0.76 \pm 0.37$ | $0.26 \pm 0.20$ |

Table 5
The execution times for the different registration techniques on a Hewlett-Packard 9000/C200 workstation for 2D ($256 \times 256$) and 3D ($128 \times 128 \times 128$) image data

| | LS | RLS | MI | IU | RIU |
|---|---|---|---|---|---|
| 2D | 30 s | 30 s | 40 s | 40 s | 1 min |
| 3D | 8 min | 8 min | 16 min | 14 min | 24 min |

patrimony [4] may benefit from the robustness of these methods.

## Acknowledgements

This study has been supported by the Commission of the European Communities, DG XII, in the framework of the TMR program (Training and Mobility of Researchers), contract Nr ERBFMIBCT960701 and by the "Groupement d'Intérêt Scientifique-Sciences de la Cognition" (CNRS, CEA, INRIA, MENESR).

The authors wish to thank Dr. Denis Bruckert (Groupement de Recherche en Télédétection et Radiométrie, LSIIT) for providing the NOAA images and Dr. Izzie-Jacques Namer (IPB) for providing and interpreting the MR and SPECT data.

## References

[1] L.G. Brown, A survey of image registration techniques, ACM Comput. Surveys, 1992 24 (4) (1992) 325–376.
[2] M. Herbin A. Venot J.Y. Devaux E. Walter F. Lebruchec L. Dubertet J.C. Roucayrol, Automated registration of dissimilar images: application to medical imagery, Comp. Vision Graphics Image Process 47 (1989) 77–88.
[3] J.R. Jensen, Introductory Digital Image Processing: A Remote Sensing Perspective, Prentice-Hall, Englewood Cliffs, NJ, 1995.
[4] F. Heitz, H. Maître, C. de Couessin, Event detection in multisource imaging: application to fine arts painting analysis, IEEE Trans. Acoust. Speech Signal Process. 38 (4) (1990) 695–704.
[5] R.P. Woods, J.C. Mazziota, S.R. Cherry, MRI-PET registration with automated algorithm, J. Comput. Assisted Tomography 17 (4) (1993) 536–546.
[6] F. Maes, A. Collignon, D. Vandermeulen, G. Marchal, P. Suetens, Multimodality image registration by maximization of mutual information, IEEE Trans. Med. Imaging 16 (2) (1997) 187–198.
[7] W. Wells III, P. Viola, H. Atsumi, S. Nakajima, R. Kikinis, Multimodal volume registration by maximization of mutual information, Med. Image Anal. 1 (1) (1996) 33–51.
[8] C. Studholme, D. Hill, D. Hawkes, Automated three-dimensional registration of megnetic resonance and positron emission tomography brain images by multiresolution optimization of voxel similarity measures, Med. Phys. 24 (1) (1997) 25–35.
[9] N.M. Alpert, D. Berdichevsky, Z. Levin, E.D. Morris, A.J. Fischman, Improved methods for image registration, Neuroimage 3 (1996) 10–17.
[10] G.E. Christensen, M.I. Miller, M.W. Vannier, U. Grenander, Individualizing neuro-anatomical atlases using a massively parallel computer, IEEE Comput January (1996) 32–38.

[11] J. Hajnal, N. Saeed, E. J. Soar, A. Oatridge, I.R. Young, G.M. Blyder, A registration and interpolation procedure for subvoxel matching of serially acquired MR images, J. Comput Assisted Tomography 19 (2) (1995) 289–296.
[12] P. Van den Elsen, J.B.A. Maintz, E.J.D. Pol, M.A. Viergever, Automatic registration of CT and MR brain images using correlation of geometrical features, IEEE Trans Med. Imaging 14 (2) (1995) 384–396.
[13] B.A. Ardekani, M. Braun, B.F. Hutton, I. Kanno, H. Iida, A fully automatic multimodality image registration algorithm, J. Comput. Assisted Tomography 19 (4) (1995) 615–623.
[14] J. Sato, R. Cipolla, Image registration using multi-scale texture moments, Image Vision Comput. 13 (5) (1995) 341–353.
[15] M.E. Alexander, R.L. Somorjai, The registration of MR images using multiscale robust methods, Magnetic Resonance Imaging 14 (5) (1996) 453–468.
[16] P.J. Rousseeuw, Least median of squares regression, J. Am. Statis. Assoc. 79 (1984) 871–880.
[17] P. Meer, D. Mintz, A. Rosenfeld, D.Y. Kim, Robust regression methods for computer vision: a review, Int. J. Comput. Vision 6 (1) (1990) 59–70.
[18] C. Stewart, Bias in robust estimation caused by discontinuities and multiple structures, IEEE Trans. Pattern Anal. Mach. Intell. 19 (8) (1997) 818–833.
[19] M.J. Black, A. Rangarajan, On the unification of line processes, outliers rejection and robust statistics in early vision, Int. J. Comput. Vision 19 (1) (1996) 57–91.
[20] J. Huber, Robust Statistics, Wiley, New York, 1981.
[21] J.M. Odobez, P. Bouthemy, Robust multiresolution estimation of parametric motion models, J. Visual Commun. Image Representation 6 (4) (1995) 348–365.
[22] M.J. Black, A.D. Jepson, Eigen Tracking: Robust matching and tracking of articulated objects using a view-based representation. Proc. European Conf. on Computer Vision, Cambridge, UK April 1996, pp. 1–14.
[23] P. Charbonnier, L. Blanc-Feraud, G. Auber, M. Barlaud, Deterministic edge-preserving regularization in computed imaging, IEEE Trans. Pattern Anal. 6 (2) (1997) 298–311.
[24] M. Black, P. Anandan, The robust estimation of multiple motions: parametric and piecewise-smooth flow fields, Comp. Vision Image Understanding 63 (1) (1996) 75–104.
[25] F. Heitz, P. Perez, P. Bouthemy, Multiscale minimization of global energy functions in some visual recovery problems, Comp. Vision Graphics Image Process. Image Understanding 59 (1) (1994) 125–134.
[26] S. Geman, D. Geman, Stochastic relaxation, Gibbs distribution and the bayesian restoration of images, IEEE Trans. Pattern Anal. Mach. Intell. 24 (3) (1984) 721–741.
[27] J. Besag, On the statistical analysis of dirty pictures, J. Roy. Statist. Soc. 48 (3) (1986) 259–302.
[28] D. Terzopoulos, Image analysis using multigrid relaxation methods, IEEE Trans. Pattern Anal. Mach. Intell. 8 (2) (1986) 129–139.

**About the Author**—CHRISTOPHOROS NIKOU was born in Thessaloniki (Greece) in 1971. He obtained the diploma in Electrical Engineering from the Aristotle University of Thessaloniki in 1994 and the DEA "Photonique et Image" from the Louis Pasteur University of Strasbourg (France) in 1995. He is currently a Ph.D. candidate at the Louis Pasteur University of Strasbourg (Image Processing, Remote Sensing and Computer Science Laboratory, LSIIT UPRES-A CNRS 7005) and at the Institute of Biological Physics (IPB UPRES-A CNRS 7004) of the Faculty of Medicine (Strasbourg University Hospital). His research interests are computer vision, pattern recognition, biomedical image processing, image registration, deformable models, stochastic signal processing. C. Nikou is a member of the IEEE and the SPIE.

**About the Author**—FABRICE HEITZ obtained the engineering degree in Electrical Engineering and Telecommunications from "Telecom Bretagne"', France, in 1984 and received the Ph.D. degree from "Telecom Paris", France, in 1988. From 1988 until 1994, he was employed by INRIA Rennes as a senior researcher in Image Processing and Computer Vision. He is now a Professor at ENSPS/LSIIT (Ecole Nationale Superieure de Physique, Image Processing, Remote Sensing and Computer Science Laboratory, LSIIT UPRES-A CNRS 7005 Strasbourg, France). F. Heitz is associate editor for the IEEE Transactions on Image Processing. His research interests include statistical image modelling, image sequence analysis and biomedical image processing.

**About the Author**—JEAN-PAUL ARMSPACH obtained the engineering degree in 1978 and the Ph.D. degree in Electrical Engineering in 1982 both from INSA Lyon, France. He is currently a research engineer at the Institut of Biological Physics, Strasbourg University Hospital, Faculty of Medicine (IPB UPRES-A CNRS 7004). His ressearch interests are Magnetic Resonance Imaging and biomedical image processing.